Switchable hidden spin polarization and negative Poisson's ratio in two-dimensional antiferroelectric wurtzite crystals

Zhuang Ma[1, ‡], Jingwen Jiang[1, ‡], Gui Wang[1], Peng Zhang[1], Yiling Sun[1], Zhengfang Qian[1], Jiaxin Zheng[2], Wen Xiong[3], Fei Wang[4], Xiuwen Zhang[1, 5], and Pu Huang[1, †]

[1]Key Laboratory of Optoelectronic Devices and Systems of Ministry of Education and Guangdong Province, College of Physics and Optoelectronic Engineering, Shenzhen University, Shenzhen 518060, China

[2]School of Advanced Materials, Peking University, Shenzhen Graduate School, Shenzhen 518055, China

[3]Chongqing Institute of Green and Intelligent Technology, Chinese Academy of Sciences, Chongqing 400714, China

[4]School of Physics and Microelectronics, Zhengzhou University, Zhengzhou 450001, China

[5]Renewable and Sustainable Energy Institute, University of Colorado, Boulder, Colorado 80309, USA

Abstract: Two-dimensional (2D) antiferroelectric materials have raised great research interest over the last decade. Here, we reveal a type of 2D antiferroelectric (AFE) crystal where the AFE polarization direction can be switched by a certain degree in the 2D plane. Such 2D functional materials are realized by stacking the exfoliated wurtzite (*wz*) monolayers with "self-healable" nature, which host strongly coupled ferroelasticity/antiferroelectricity and benign stability. The AFE candidates, i.e., ZnX and CdX (X = S, Se, Te), are all semiconductors with direct bandgap at Γ point, which harbors switchable antiferroelectricity and ferroelasticity with low transition barriers, hidden spin polarization, as well as giant in-plane negative Poisson's ratio (NPR), enabling the co-tunability of hidden spin characteristics and auxetic magnitudes via AFE switching. The 2D AFE *wz* crystals provide a platform to probe the interplay of 2D antiferroelectricity, ferroelasticity, NPR, and spin effects, shedding new light on the rich physics and device design in *wz* semiconductors.

Key words: wurtzite crystal; multiferroics; hidden spin polarization; negative Poisson's ratio

1. Introduction

Antiferroelectric (AFE) materials have identifiable spontaneous dipole moments arranged in an antiparallel ordering within two sublattices of the same magnitude, leaving a net-zero macroscopic polarization for the crystal structure at zero electric field. The notion of antiferroelectricity dates to the early-1950s, as is theoretically justified by Kittel[1] and experimentally evidenced by Shirane and Sawaguchi with classical AFE perovskite $PbZrO_3$[2–4]. During the past decades, AFE materials have garnered significant research interest due to their potential applications in information and energy storage[5, 6]. Unlike the ferroelectric (FE) materials, which exhibit a single polarization-electric field (P-E) hysteresis loop achieved by reversing the spontaneous polarization, AFE materials undergo a distinctive AFE phase transition characterized by a double P-E hysteresis loop. This unique behavior gives rise to a remarkable volume change and considerable dielectric polarization enhancement, enhancing their suitability for diverse applications[7]. One significant advantage of AFE materials over FE counterparts lies in the absence of remnant polarization, rendering the need for pre-poling processes unneces-

sary[8]. This feature simplifies device fabrication and facilitates their integration into storage capacitors with high energy density and high breakdown voltages[9–11], decoupling capacitors in high-speed multichip modules, and energy conversion devices[12]. AFE materials also hold promise for energy conservation and multiferroic devices because they demonstrate considerable strain/stress tolerance compared to conventional FE materials[6]. Additionally, their swift switching between AFE and FE phases makes them indispensable for electronic devices requiring rapid response times and high-frequency operation[13]. Furthermore, the net-zero macroscopic polarization characteristics of AFE materials confer benign resistance to external electric fields, contributing to the increased durability of electronic components.

Searching for optimal AFE materials is now in full swing, especially the urgent demand for AFE semiconductors with diversity, novelty and superiority in the post-Moore era[14]. Although many two-dimensional (2D) FE materials have been discovered recently (e.g., In_2Se_3[15], $CuInP_2S_6$[16], phosphorene and its analogs[17], etc.), few of 2D AFE materials have been reported. Only several van der Waals (vdW) materials[13, 18–20], inorganic metallic oxides[21–23], and organic-inorganic hybrid perovskites[24–26] have been proposed as 2D AFE materials, among which most experimentally available candidates are macromolecular lead-based perovskites. The inclusion of lead (toxicity) and macromolecules is detrimental to the manufac-

turing of environmentally-friendly micro-miniature devices. In addition, the previous theory-proposed 2D AFE materials present metallic feature or indirect band structures (Table S1), which is not conducive to fabricate high-performance semiconductor devices. Therefore, the rational design of 2D AFE materials with tunable properties, extraordinary electronic characteristics, and process compatibility in modern 2D semiconductor technology is still challenging.

Inspired by the innate capacity for autonomous structural recovery[27], self-healable materials offer a novel paradigm for designing ferroic structure, wherein the system's polarization can be modulated during the self-healing process. Usually, the approaches to self-healing have utilized physical and chemical processes, or a combination thereof, which includes but are not limited to covalent bond or vdW interaction reformation. For instance, investigations have explored the feasibility of leveraging the self-healing property for depositing monolayer MoS_2 on SiO_2 surfaces[28] and constructing MoS_2 vdW homojunctions[29]. For the non-vdW non-centrosymmetric (non-CS) materials, such as wurtzite (*wz*) crystal, the deposition of its monolayer [exfoliated from (110) surface] can lead to the restoration of the *wz* structure through the self-healing of local motifs from triangles to tetrahedra, wherein off-centered cation bonds with anions to form energetically favorable tetrahedral configurations[30]. Notably, if the polarization direction between the *wz* monolayer and pristine surface is opposite, then the polarization of the entire system could be partially or completely quenched. Consequently, manipulating the motif configuration and arrangement via self-healing process is a viable strategy for designing new antiferroelectric or ferrielectric structures.

In this work, we reveal a class of 2D antiferroelectric (AFE) *wz* crystal with switchable ferroelasticity and antiferroelectricity by stacking the *wz* monolayer[30], where the AFE polarization direction can be switched by a certain degree in the 2D plane. The prototypes of 2D *wz* ZnX and CdX (X = S, Se, Te) are all semiconductors possessing low multiferroic transition barriers, leading to tunable hidden spin polarization around the valence band maximum (VBM) and giant in-plane negative Poisson's ratio (NPR). Our study realizes the synergy of multiferroic, hidden spintronic and auxetic characteristics in 2D AFE *wz* crystal and provides a new platform of 2D AFE semiconductors for further investigations on the physical properties, as well as device design.

2. Results and discussion

2.1. Building the 2D AFE *wz* crystal

AFE materials belong to the centrosymmetric (CS) and non-polar symmetry, whose AFE polarization can be reversed through flipping the built-in electric field, indicating the parallel AFE phase transition along the polarization direction. We note that if the AFE polarization direction can be rotated by a certain degree (e.g., $\pm\pi/2$ perpendicular to the pristine polarization direction), then several other AFE structures would occur. Benefiting from the structural manipulation freedoms (e.g., interlayer rotation/sliding[31, 32]) and large strain tolerance[33], 2D materials would act as the favorable block to build the AFE structure. Among them, 2D out-of-plane FE polarization can be switched by in-plane interlayer sliding of stacking the nonpolar 2D materials[34−36]. Aiming to integrate
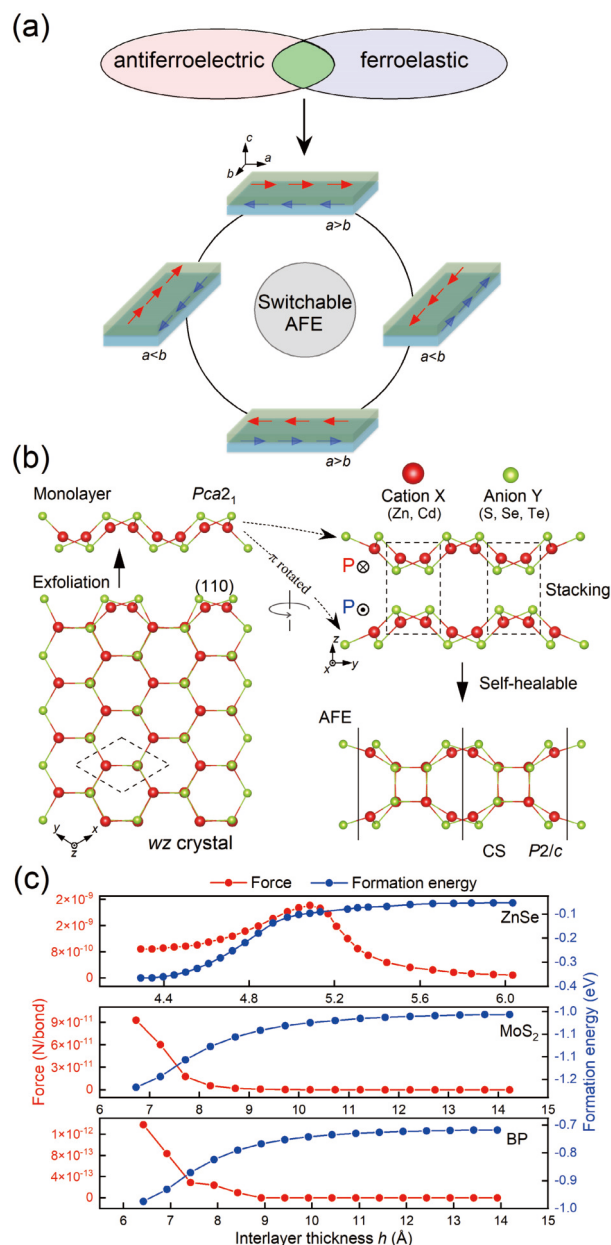

Fig. 1. (Color online) (a) Schematic depiction of how the ferroelastic-antiferroelectric is induced from antiferroelectricity and ferroelasticity, in which the red and blue arrows indicate the FE polarization for each sector of the system. (b) Building the 2D AFE structures (cation X = Zn, Cd; anion Y = S, Se, Te, *P2/c* symmetry) with the *wz* monolayer (*Pca*2₁ symmetry) as building blocks. Here, the *wz* monolayer is exfoliated from the *wz* bulk thick layer with (110) crystallographic plane, which can bond spontaneously with another one when stacked vertically due to the inherent self-healable nature. (c) The average interlayer force (per bond in unit cell) and formation energy as a function of the slab thickness h in the 2D AFE ZnSe, 2L MoS_2 and 2L black phosphorene, respectively.

the orientation-dependent AFE polarization in one 2D system, we evaluated the structural deformation properties of 2D materials and realized that the combination of antiferroelectricity and ferroelasticity is an optimal manner to achieve the phase transition characteristics owing to the orientation-dependent states via a ferroelastic (FC) switch (Fig. 1(a)). Subsequently, we chose the *wz* ferroelectrics to build the 2D AFE structure by virtue of its switchable polarization[37] and self-

healable nature within the 2D limit[30]. The FE polarization is inherent in the *wz* monolayer as the preserved net non-zero polarization along the polar *c*-axis of the bulk due to the non-centrosymmetric (non-CS) symmetry. When two *wz* monolayers are stacked with π rotated degrees between each other, the emergence of interlayer reconstruction would transform the structure into a CS AFE phase after the self-healing process because the opposite dipole polarization between the two layers can be cancelled for the entire system (Fig. 1(b)). Here, all the possible stacking patterns for the two FE layers have been considered (Figs. S1(a) and S1(b)), which yields the most stable configuration of the selected AFE structure. The AFE unit cell belongs to $P2/c$ symmetry (SG: 13) and contains eight cations (Zn or Cd) and eight anions (S, Se, or Te), respectively. Taking ZnSe as the representative, the Zn and Se atoms on the top and bottom surfaces form triangles connected by vertices, while the mid-positioned counterparts form pairs of nested tetrahedra. This local motif arrangement facilitates the stability of the structure because the phonon spectra present the non-imaginary-frequency feature and the *ab initio* molecular dynamics (AIMD) simulation keeps the same phase structure in the simulated time, proving the stable state (Figs. S2 and S3).

We studied the self-healing process of the 2D AFE crystal by evaluating the interlayer interaction force F, which is expressed by the formula

$$F = -\frac{\partial E}{\partial h}. \quad (1)$$

The denominator h presents the interlayer thickness and the numerator E denotes the averaged atomic interaction strength[38]:

$$E = \sum_{R,L} \sum_{R',L'} H_{R,L,R',L'} n_{R,L,R',L'}, \quad (2)$$

where the subscript R and L are the atom sites and electronic orbitals for selected atoms, respectively. H is the Hamiltonian matrix $\langle \psi_{R,L} | \bar{H} | \psi_{R',L'} \rangle$ and n presents the density matrix element by integrating the density of states to Fermi level. The calculated force F and formation energy ($E_{FAFE} - 2 \times E_{monolayer}$) for AFE ZnSe are shown in Fig. 1(c), in which we provide the 2L MoS$_2$ and black phosphorene as comparison. The formation energies for all of them gradually decrease and converge to stable states. Nevertheless, a significant difference can be found from the perspective of F because the value of ZnSe increases to the critical point (h = 5.09 Å) and then undergoes a rapid decline, which originates from the atomic self-healing reconstruction at the interface. The broken triangle in the basal plane increases the $s-p$ bonding orbital coupling between the off-centered cation (moving out of the anion triangle center) and the nearest anions positioned at the vertex of the other layer (Fig. S4), which leads to the drop of the force due to the local motif transformation from triangle to tetrahedra. Therefore, compared with the formation energy, the interaction force F could act as a more sensitive quantity to monitor the local structure evolution of the entire system.

2.2. Phase transition of the 2D AFE *wz* crystal

We found that ferroelasticity can be endowed within these 2D AFE structures because the atomic movements between each layer give rise to the multiferroic (coupled antiferroelectricity and ferroelasticity) switching of the AFE structure, forming four accessible AFE phases (AFE-n, $n \in [1, 2, 3, 4]$). For instance, denoting the initial ZnSe structure as AFE-1 phase (Fig. 2(a)), when the Se atoms in the upper and lower monolayers move linearly along the FE transition path[30], the triangle will transform into tetrahedra, and the structure will evolve into the CS$_1$ $C2/m$ phase. If the tetrahedra experience $b/4$ interlayer gliding along lattice b direction, then the structure would transform into CS$_2$ $P4/nmm$ phase. Then, three sub-paths could be found for the subsequent movement of Se atoms. First, continuingly moving along the linearly initial path with $b/4$ distance, the structure will return to the $C2/m$ phase. The tetrahedra will then transform into a triangle with the structure restoring the AFE configuration (AFE-2) but will possess opposite dipole polarization for the upper and lower layers compared with the initial AFE-1 situation. Second, if the tetrahedra of the CS$_2$ $P4/nmm$ phase rotates with π/2 degree (perpendicular to the initial linear path), then the structure will undergo a FC phase transition to AFE-3 due to the π/2 rotated dipole polarization for the structure. Finally, for the -π/2 degree gliding path, the structure will transform into AFE-4 and possess opposite polarization compared with AFE-3. In other words, the AFE-n configurations are bridged smoothly through the CS$_1$ and CS$_2$ phases, which leads to the switchable transition between these four AFE structures.

We evaluated the energy barrier between the AFE and CS$_{1/2}$ phases, as shown in Figs. 2(b) and 2(c). Because of the symmetry, the reaction path from either AFE-n configuration to another through the CS$_1$ and CS$_2$ phases are identical. The total energies of ZnS and CdS with AFE phase are lower than that of the CS$_1$ and CS$_2$ counterparts, leading to a large transition barrier (ΔE_1 = 0.205/0.190 eV/f.u., ΔE_2 = 0.051/0.026 eV/f.u.) during the AFE-m/CS$_1$/CS$_2$/AFE-n transition process (m, n = 1, 2, 3, 4; ΔE_1 and ΔE_2 denote the barrier heights for the AFE-$m \rightarrow$ CS$_1$ and CS$_1 \rightarrow$ CS$_2$ phase changing route). In contrast, the total energy differences of ZnSe and CdSe between the AFE and CS phases are relatively small, presenting low transition energy barriers (ΔE_1 = 0.103/0.118 eV/f.u., ΔE_2 = 0.063/0.041 eV/f.u.). For ZnTe and CdTe, the CS phases' total energy further decreases, thus forming a low-lying energy land with respect to the AFE horizontal (ΔE_1 = 0.048/0.058 eV/f.u., ΔE_2 = 0.066/0.053 eV/f.u.). Here, the negative energy in the NEB pathway indicates that the CS$_2$ $P4/nmm$ phases of ZnTe and CdTe are ground states because they present slightly lower energies compared with the $P2/c$ phase (0.03 and 0.01 eV/f.u. lower for ZnTe and CdTe, respectively). Overall, the barrier height (beyond the room temperature fluctuation k_BT) and the required external strain for these AFE phase transitions are moderate, which ensures the AFE switching. The ferroelastic switching can have an identical height as the AFE transition. Such ferroelastic phase transition in 2D AFE *wz* crystals could be induced by external strain analogous to the strain triggered FC transition in 2D β'-In$_2$Se$_3$[39], or by high-order electric field analogous to the FC transition of SnO, SnSe, and Bi (110) monolayers by applying an alternating electric field[40, 41]. The high-order electric field could strongly couple with the local dipole moments in the 2D AFE *wz* crystals, inducing an FC transition by switching the direction of local electric polarization.
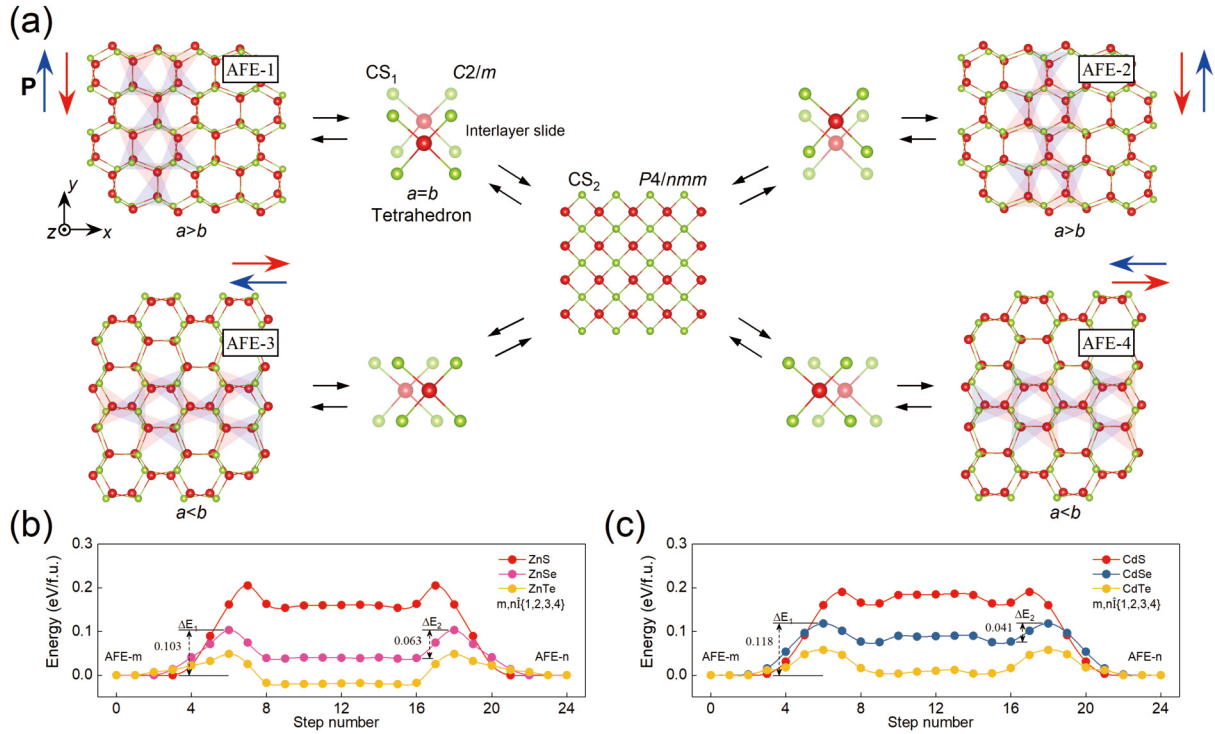
Fig. 2. (Color online) (a) Feasible phase transition channels for the 2D AFE structure. The triangle in either AFE-1/2/3/4 structure can transform into tetrahedra with the phase transition into CS$_1$ $C2/m$ structure, which further changes into CS$_2$ $P4/nmm$ structure due to the interlayer slipping for tetrahedra ($a/4$ or $b/4$ along the lattice direction). The continuing movement of the tetrahedra would make the structure restore the AFE phase through the $C2/m$ structure, forming the AFE phase changing channel with π (inversed) or π/2 rotated triangle configurations. Here, the blue and red arrows denote the polarization direction within each layer of the AFE-n structure, as accentuated by the congruent hues presenting in the corresponding triangles. (b), (c) Phase changing barrier for the 2D AFE structures, where the ΔE_1 and ΔE_2 depict the barrier heights for the AFE-$m,n \to$ CS$_1$ and CS$_1 \to$ CS$_2$ phase changing process.

Table 1. Lattice constants a and b (Å), FC reversible strains ε (%), band gaps (eV) with PBE and HSE06 functionals, transition barrier ΔE_1 (eV/f.u.) for AFE-$m,n \to$ CS$_1$ and ΔE_2 (eV/f.u.) for CS$_1 \to$ CS$_2$ phase changing process, and NPR value v along lattice direction of wz AFE structures.

Crystal	a (Å)	b (Å)	ε (%)	HSE^{SOC} (eV)	PBE^{SOC} (eV)	ΔE_1 (eV/f.u.)	ΔE_2 (eV/f.u.)	v_a	v_b
ZnS	7.39	6.55	12.8	3.76	2.60	0.205	0.051	−0.398	−0.206
ZnSe	7.63	6.81	12.0	3.02	2.00	0.103	0.063	−0.469	−0.226
ZnTe	8.12	7.26	11.8	2.65	1.82	0.048	0.066	−0.614	−0.288
CdS	7.87	7.06	11.5	2.82	1.85	0.190	0.026	−0.192	−0.099
CdSe	7.98	7.25	10.1	2.35	1.52	0.118	0.041	−0.296	−0.131
CdTe	8.08	7.47	8.2	2.17	1.47	0.058	0.053	−0.536	−0.233

We further evaluated the FC signal intensity of the 2D AFE wz crystals by using the reversible strain ε in Table 1, which is defined as $\varepsilon = (|a| / |b| - 1) \times 100\%$. For 2D AFE ZnS crystal, the reversible strain is as large as 12.8, i.e., the in-plane lattice constants are changed by 12.8% during the ferroelastic phase transition. The reversible strains are relatively smaller than the common 2D FC materials, e.g., phosphene (37.9%)[17], CrSX (X = Cl, Br, I) (22.1%−36.5%)[42], etc., which originates from the low transition barriers and indicates the accessibility of strain engineering[43, 44]. Here the FC strain, while intrinsic to the FC materials, does not directly dictate the magnitude of applied strain required for FC switching. The process of FC switching does not demand such a high level of externally applied strain because the structure transformation occurs spontaneously once the energy barrier for FC switching is surmounted. To further evaluate FC switching in the AFE phase, we employed the transformation strain matrix η, taking the intermediate state CS$_2$ phase as a reference state. Based on the Green−Lagrange strain tensor[45], the matrix can be expressed as

$$\eta = \frac{1}{2}\left[(H_P^{-1})^{T} H_I^{T} H_I H_P^{-1} - I\right]. \tag{3}$$

Here the superscript −1 indicates the matrix inversion, T denotes matrix transpose, I is a 2 × 2 identity matrix, and H_I and H_P represent the matrices of the state I and the intermediate state CS$_2$, respectively. For AFE ZnS, the matrices H_I and H_P are [7.39, 0; 0, 6.55] and [6.97, 0; 0, 6.97]. η is calculated to be [0.062, 0; 0, −0.058], suggesting a 6.2% stretch strain along the a-direction and a 5.8% compressive strain along the b-direction. This assessment sheds light on the strain distribution critical for AFE polarizations switching. It is noteworthy that 2D materials usually exhibit significant strain tolerance, exemplified by graphene (⩾25%)[46], MoS$_2$ (11%)[47], and black phosphorus (9.2%)[48].
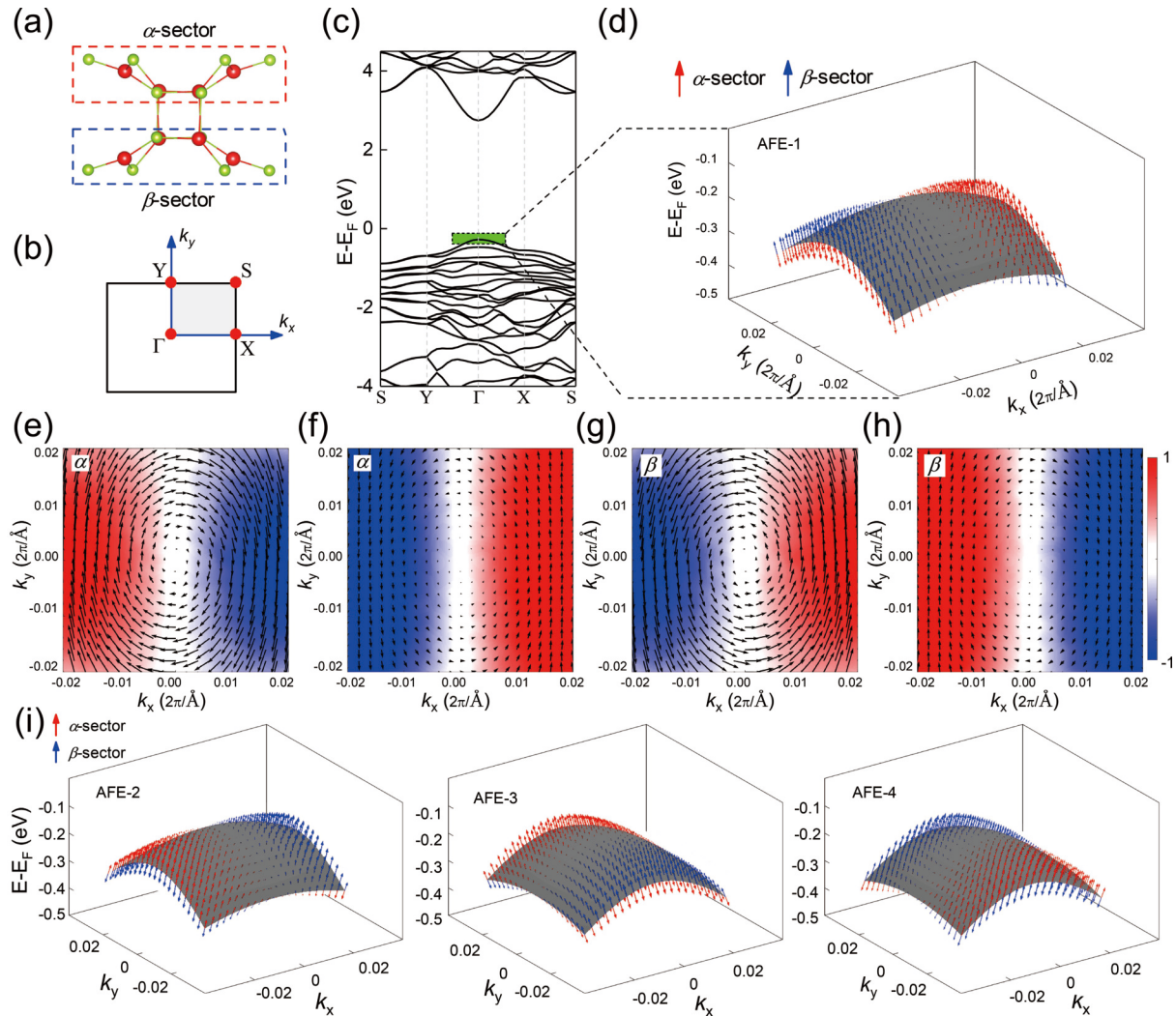
Here the facile interlayer gliding (almost zero transition

Fig. 3. (Color online) (a) Crystal structure for 2D AFE ZnSe with boxed α-sector and β-sector for hidden spin projection. (b) The first Brillouin zone of the 2D AFE structure, where the high symmetry k points (Γ, X, Y, and S) are indicated. (c) Band structure (HSE06 + SOC) for 2D AFE ZnSe. (d) 3D spin texture near the VBM region highlighted in (c), in which the red and blue arrows indicate the spin polarization contributed by α- and β-sector and the magnitude of spin vectors depend on the strength of SOC and spin splitting. Corresponding 2D diagram of the spin polarizations of α-sector (e), (f) and β-sector (g), (h) and the color scheme indicates the out-of-plane spin component, the shade of color bar represents the magnitude of the hidden spin polarization. (i) Switchable spin texture projected to the k space for the 2D AFE ZnSe around VBM, which is expected by tuning the in-plane AFE polarization.

barrier for $CS_1 \rightarrow CS_2$ phase changing route) of the tetrahedra between CS_1 and CS_2 phases originates from the converted orbital interaction from the bonding state in AFE phase to the vdW interaction of the interlayer atoms, e.g., exchanging the nearest interlayer atomic bonding pair from Zn−Se to Se−Se. Therefore, the dominating interlayer bonding interaction of ZnSe AFE configuration (−ICOHP: 1.10) can be converted into vdW form (−ICOHP: 0.033 and 0.030) for CS_1 and CS_2 structures, which are much smaller than that of common vdW materials, e.g., MoS_2 (0.079) and black phosphorus (0.091), confirming the weak vdW interaction between the layers of CS_1 and CS_2 phases. Moreover, the energy landscape for the interlayer tetrahedra gliding exhibits negligible energy variation (Figs. S1(c) and S1(d)), indicating the energy-favorable interlayer gliding with few constraints.

2.3. Switchable hidden spin polarization through AFE transition

In consideration of the hidden spin characteristics induced by non-CS site symmetries and spin-orbit coupling

(SOC)[49], we investigated the electronic structure of these 2D AFE wz crystals. Our findings reveal that all the AFE phases are semiconductors with direct band gaps located at the Γ point of Brillouin zone (Fig. S5). Although the entire spin splitting cannot be realized by introducing the SOC due to the preserved inversion symmetry, the individual part (α or β) of the AFE structure presents opposite hidden spin polarization character (Fig. 3(a)), which is mainly visible at the VB bands along the Y−Γ−X high-symmetry lines (e.g., AFE-1 structure of ZnSe in Figs. 3(b) and 3(c)). The α sector with structural polarization along y direction presents ↑ and ↓ spin orientation for Y−Γ−X region, while the β sector with structural polarization along −y direction possesses opposite ↓ and ↑ spin characteristics (Fig. 3(d)). We plot the 2D diagram of the spin polarizations of α/β sector and find a uniform pattern of the spin texture around the Γ point (Figs. 3(e)−3(h)), which is verified as hidden 1D Rashba-type spin characteristics. Since the electronic states near the Fermi level are important for carrier transport and optical transition behavior, the emergence
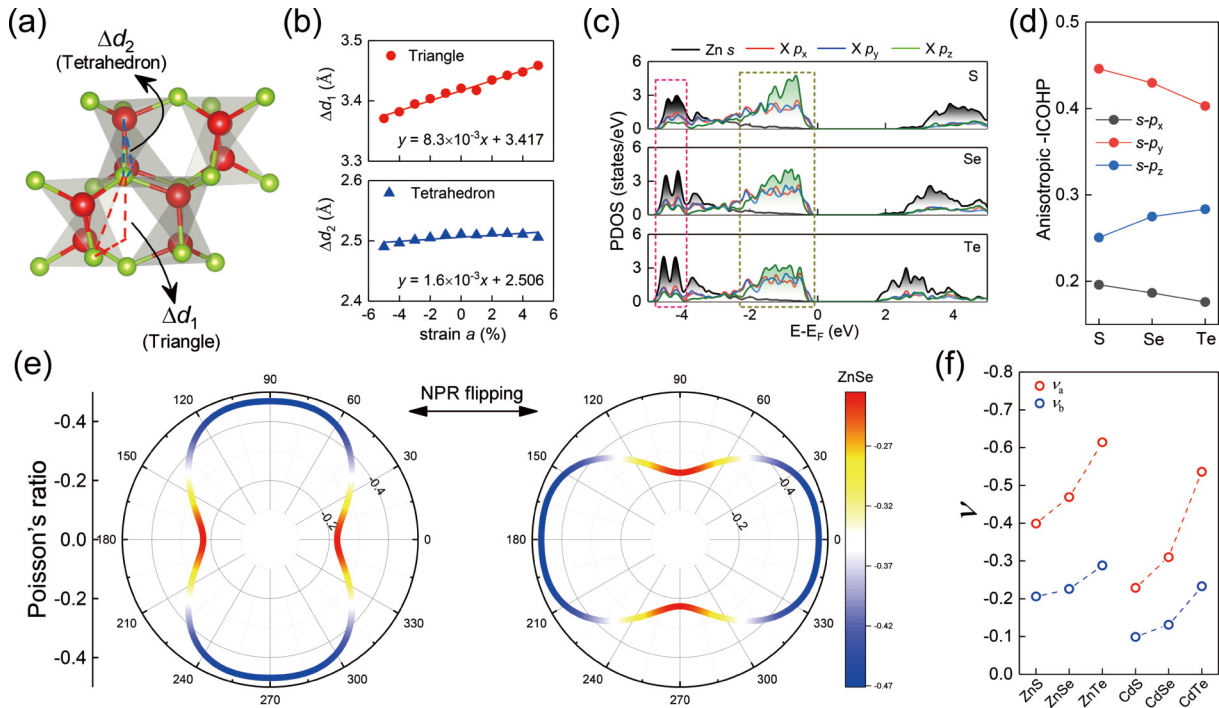
Fig. 4. (Color online) (a) Top view for ZnSe AFE structure, in which we denote the projections of triangle and tetrahedra along b-axis by Δd_1 and Δd_2, respectively. (b) Variation of the Δd_1 and Δd_2 with strain along lattice a. (c) PDOS for the ZnX (X = S, Se, Te), indicating the localized/dispersive cation s/anion p state. (d) Anisotropic in-plane s-$p_{x/y}$ and out-of-plane s-p_z orbital interactions in ZnX. (e) In-plane NPR response for 2D AFE ZnSe, which can be flipped through the AFE transition. (f) Statistical NPR values for the 2D AFE structures, among which three members have NPR exceeding −0.450.

of the hidden spin polarization around VBM (Γ point) region for the 2D AFE wz crystals facilitates the future experimental probing, e.g., using the spin angle-resolved photoemission spectroscopy (ARPES)[50–52]. When the AFE structure transforms from one phase to another, the hidden spin polarization can also be flipped due to the switching of the ferroelectricity for the α and β sector layers, which can be seen in Figs. 3(d)–3(i) for the momentum-resolved spin texture of the four ZnSe AFE phases. Switchable hidden 1D Rashba-type spin texture projected onto the k space for the α and β sectors of AFE ZnSe around VBM are expected by reversing the in-plane polarization with π and ±π/2 degrees through the AFE phase transitions.

2.4. Flipping the negative Poisson's ratio in 2D AFE wz crystal

Another intriguing property of the proposed 2D AFE structure is the giant in-plane NPR, which is associated with the unique stacking pattern of triangular local motifs at the upper and lower surfaces[30]. The NPR's strength is slightly decreased compared with the wz monolayer because the atoms reconstruct from triangle to tetrahedra at the middle region (the CS_1 and CS_2 phase with tetrahedra present no NPR response). The mechanism is investigated in detail as follows. From the perspective of geometric dimensionality, the lattice $y(b)$ is determined by the projection of triangle (Δd_1) and tetrahedra (Δd_2) along the b-axis [strain along lattice $x(a)$] (Fig. 4(a)). Both the Δd_1 and Δd_2 enlarge with increasing strain value; nevertheless, the slope magnitudes are different because the former is almost seven times larger than the latter (Fig. 4(b)), which indicates the significant suppression of NPR strength in tetrahedra coordination environment. For

the electronic dimensionality, the integration of −ICOHP for the local atoms of triangle and tetrahedra are 3.14 and 5.14, respectively, suggesting vigorous counteraction of the tetrahedra to the structural deformation during the mechanical stretch. The NPR trend of the 2D AFE materials shows: ZnS < ZnSe < ZnTe; CdS < CdSe < CdTe, as can be seen from the anisotropic bonding orbital coupling of s and p states. The s–$p_{x/y}$ coupling is weakened but the s–p_z counterpart is strengthened gradually, which facilitates the structural expansion due to the opposite in- and out-of-plane orbital interactions (Figs. 4(c) and 4(d)). As shown in Table 1, three kinds of 2D AFE crystals (ZnSe, ZnTe, CdTe) have giant NPR values exceeding −0.450, among which ZnTe presents an enormous value of −0.614. Moreover, we emphasized that the NPR values v for the 2D AFE wz crystal present significant anisotropy, which can be flipped through the AFE phase transition (Figs. 4(e) and 4(f)) and Fig. S6.

3. Conclusion

We would finally like to discuss the significance of 2D AFE wz crystals and the compatibility of these candidates with modern 2D semiconductor technology. Comparing with the currently reported 2D hidden spin materials, e.g., $PtSe_2$ (indirect band gap)[53], 1T MX_2 (M = Zr, Hf; X = S, Se, Te) (small band gap)[54], $BaNiS_2$ (present impurity electronic states around the Fermi level)[55], and $LiBiO_2$ (doubly degenerate states at the band edge)[21], our proposed 2D AFE candidates present the semiconductor feature with a clean and broad energy gap (2.17–3.76 eV), which is not only desirable for the device application but also facilitates the detection and modulation of hidden spin effect[56, 57]. Furthermore, during the device preparation process, lattice mismatch (η)

between the material and substrate is crucial because the significant mismatch usually induces interface defects, e.g., vacancies, anti-site substitutions and interstitials in WSe$_2$/h-BN[58], dislocation for epitaxial ZnSe on ZnS[59], and low-angle grain boundaries for WSe$_2$ and MoS$_2$ superlattice[60], thus weakening the performance of the device. Additionally, the interaction between the substrate and the host should be sufficiently weak to eliminate the influence from the substrate, e.g., interface distortion and chemical bonding. We evaluated the η values of the 2D AFE wz crystals with commonly used 2D substrates (Table S2), which suggests that most of them present benign lattice matches, such as AFE ZnSe on the graphene (3.0% to −4.5%), 2H-MoS$_2$ (−1.1% to −4.0%), and h-BN (1.3% to 4.4%). The interactions between them are vdW form with −ICOHP: 0.0017, 0.0025, and 0.0040, respectively, which are one order of magnitude lower than that of MoS$_2$ and phosphorene (~0.08−0.1). Moreover, the 2D AFE wz crystals possess favorable auxiticity and could endure significantly larger lattice strain compared with the bulk counterparts, e.g., the stable phonon (±5% strain along lattice a or b, Fig. S7) can be preserved for strained ZnSe (the wz bulk usually would withstand up to 4% strains, e.g., wz GaN)[61]. Recognizing the significance of local polarization as a key determinant influencing the subsequent device performance, we conducted an evaluation of the magnitude of local polarization for AFE ZnX and CdX (X = S, Se). The local max polarization (P_{max}) in each unit cell reaches up to ~1.6×10^{-10} C/m, which is comparable to the other 2D AFE compounds such as Bi monolayer (1.4×10^{-10} C/m)[62], single-layer γ-AlOOH (0.85×10^{-10} C/m)[63], and nanostripe-ordered In$_2$Se$_3$ (~0.26×10^{-10} C/m)[20].

We note that 2D materials with non-vdW interlayer forces have been synthesized using mechanical cleavage and liquid phase exfoliation techniques recently. For instance, Geng et al. reported the exfoliation of various stable monolayer and few-layer structures (e.g., Bi, SnO, and KV$_3$Sb$_5$) with metal, semiconductor, and superconducting properties from inorganic layered structures with non-vdW-type interlayer forces[64]. Similarly, Ajayan et al. demonstrated the feasibility of obtaining 2D materials with different crystallographic planes by means of liquid exfoliation of common iron ore, thereby obtaining a material called "hematene" with promising applications in visible light photocatalysis[65]. Additionally, Chang et al. utilized a chemical vapor deposition (CVD)-assisted ultra-sonication method to exfoliate 2D ferromagnetism CrTe from non-vdW CrTe along the (002) crystal face[66]. Furthermore, recent experimental findings have indicated the fabrication of wz nanosheets with (110) plane such as InP[67], ZnS[68, 69], CdSe[70], etc. Our research also indicates the accessibility of non-vdW wz monolayer from the (110) plane of wz bulk, due to the low cleavage energy and anisotropic in-/out-of-plane bonding interactions[30]. Considering these observations, the possibility of obtaining wz monolayers has significantly increased due to the combination of experimental and theoretical approaches.

To the best of our knowledge, the 2D AFE wz crystal is the first 2D AFE candidate possessing such extraordinary properties integrated into one system (see Table S1 for the current 2D AFE materials). More importantly, the combination of ferroelasticity/antiferroelectricity, hidden spin polarization, and anisotropic NPR offers the opportunity to control the aux-

etic effect via AFE switching, which not only meets the pursuit of electric-field induced elastic deformation for AFE nonvolatile memory device with ultralow energy consumption[71] but also provides a new platform with intrinsic antiferroelectricity and ferroelasticity coupling to inspire multiple physics research and device design in the post-Moore era. For instance, the combination of antiferroelectric functional materials and microelectromechanical systems (MEMS) technology provides new paradigms for the design and development of highly sensitive intelligent sensor and phase strain effect devices under external fields (external electric field, temperature, or strain)[1, 72−77]. The thickness of conventional antiferroelectric materials is mostly as large as several hundred nanometers, which is far from the requirement of nanoscale electronics and devices[74, 75, 78]. The sub-nanometer thick 2D AFE wz crystals predicted in this study host a ferroelastic phase transition with up to 12.8% variation of lattice dimensions, which could also be controlled by high-order electric fields. This strong electromechanical effect suggests the promising applications of 2D AFE wz crystals in MEMS systems.

In summary, we realized a type of 2D AFE wz crystal by using the self-healable nature of the wz monolayer. Fine-grained phase engineering of these 2D AFE materials is evaluated to monitor the evolution of this material's electronic characteristics, which gives rise to the switchable AFE response, giant in-plane NPR, and hidden 1D Rashba-type spin characteristics. The 2D AFE candidates ZnX and CdX (X = S, Se, Te) harbor strongly coupled antiferroelectricity and ferroelasticity with low transition barriers (~0.05−0.2 eV/f.u.) and giant 2D in-plane NPR (half of them exceed −0.450). The 2D AFE wz crystals are semiconductors possessing direct band gap, enabling the co-tunability of hidden spin orientation and auxetic magnitudes. Our study provides the feasible strategy for the construction of novel 2D AFE crystals. Moreover, the insight into utilizing the extraordinary synergy for AFE property, hidden spin polarization and NPR switch successfully integrated the multiferroics, spintronics, and mechanics into one system, providing a new platform to investigate the intriguing physical properties and the new form of AFE applications.

Acknowledgements

Appendix A. Supplementary material

Supplementary materials to this article can be found online at https://doi.org/10.1088/1674-4926/44/12/122101.

References

[1] Kittel C. Theory of antiferroelectric crystals. Phys Rev, 1951, 82, 729

[2] Shirane G, Sawaguchi E, Takagi Y. Dielectric properties of lead zir-

conate. Phys Rev, 1951, 84, 476

[3]   Shirane G. Ferroelectricity and antiferroelectricity in ceramic PbZrO$_3$ containing Ba or Sr. Phys Rev, 1952, 86, 219

[4]   Sawaguchi E, Maniwa H, Hoshino S. Antiferroelectric structure of lead zirconate. Phys Rev, 1951, 83, 1078

[5]   Randall C A, Fan Z M, Reaney I, et al. Antiferroelectrics: History, fundamentals, crystal chemistry, crystal structures, size effects, and applications. J Am Ceram Soc, 2021, 104, 3775

[6]   Liu Z, Lu T, Ye J M, et al. Antiferroelectrics for energy storage applications: A review. Adv Mater Technol, 2018, 3, 1800111

[7]   Qi H, Zuo R Z, Xie A W, et al. Ultrahigh energy-storage density in NaNbO$_3$-based lead-free relaxor antiferroelectric ceramics with nanoscale domains. Adv Funct Mater, 2019, 29, 1903877

[8]   Zhou Z Y, Yang Q, Liu M, et al. Antiferroelectric materials, applications and recent progress on multiferroic heterostructures. SPIN, 2015, 5, 1530001

[9]   Narayanan M, Ma B H, Tong S, et al. Electrical properties of Pb$_{0.92}$La$_{0.08}$Zr$_{0.52}$Ti$_{0.48}$O$_3$ thin films grown on SrRuO$_3$ buffered nickel and silicon substrates by chemical solution deposition. Int J Appl Ceram Technol, 2012, 9, 45

[10] Huang B Y, Lu Z X, Zhang Y, et al. Antiferroelectric polarization switching and dynamic scaling of energy storage: A Monte Carlo simulation. J Appl Phys, 2016, 119, 174103

[11] Payne A, Brewer O, Leff A, et al. Dielectric, energy storage, and loss study of antiferroelectric-like Al-doped HfO$_2$ thin films. Appl Phys Lett, 2020, 117, 221104

[12] Bharadwaja S S N, Krupanidhi S B. Backward switching phenomenon from field forced ferroelectric to antiferroelectric phases in antiferroelectric PbZrO$_3$ thin films. J Appl Phys, 2001, 89, 4541

[13] Guan Z, Zhao Y F, Wang X T, et al. Electric-field-induced room-temperature antiferroelectric–ferroelectric phase transition in van der waals layered GeSe. ACS Nano, 2022, 16, 1308

[14] Liu C S, Chen H W, Wang S Y, et al. Two-dimensional materials for next-generation computing technologies. Nat Nanotechnol, 2020, 15, 545

[15] Ding W J, Zhu J B, Wang Z, et al. Prediction of intrinsic two-dimensional ferroelectrics in In$_2$Se$_3$ and other III$_2$-VI$_3$ van der Waals materials. Nat Commun, 2017, 8, 14956

[16] Liu F C, You L, Seyler K L, et al. Room-temperature ferroelectricity in CuInP2S6 ultrathin flakes. Nat Commun, 2016, 7, 12357

[17] Wu M H, Zeng X C. Intrinsic ferroelasticity and/or multiferroicity in two-dimensional phosphorene and phosphorene analogues. Nano Lett, 2016, 16, 3236

[18] Dziaugys A, Kelley K, Brehm J A, et al. Piezoelectric domain walls in van der Waals antiferroelectric CuInP$_2$Se$_6$. Nat Commun, 2020, 11, 1

[19] Ding J, Shao D F, Li M, et al. Two-dimensional antiferroelectric tunnel junction. Phys Rev Lett, 2021, 126, 057601

[20] Xu C, Chen Y C, Cai X B, et al. Two-dimensional antiferroelectricity in nanostripe-ordered In$_2$Se$_3$. Phys Rev Lett, 2020, 125, 047601

[21] Guan S, Luo J W. Electrically switchable hidden spin polarization in antiferroelectric crystals. Phys Rev B, 2020, 102, 184104

[22] Chen S B, Sun H S, Ding J F, et al. Unconventional distortion induced two-dimensional multiferroicity in a CrO$_3$ monolayer. Nanoscale, 2021, 13, 13048

[23] Zhao J L, Wang X Y, Chen H H, et al. Two-dimensional ferroelectric Ga$_2$O$_3$ bilayers with unusual strain-engineered interlayer interactions. Chem Mater, 2022, 34, 3648

[24] Wu Z Y, Liu X T, Ji C M, et al. Discovery of an above-room-temperature antiferroelectric in two-dimensional hybrid perovskite. J Am Chem Soc, 2019, 141, 3812

[25] Han S G, Liu X T, Liu Y, et al. High-temperature antiferroelectric of lead iodide hybrid perovskites. J Am Chem Soc, 2019, 141, 12470

[26] Li M F, Han S G, Liu Y, et al. Soft perovskite-type antiferroelectric

[27] with giant electrocaloric strength near room temperature. J Am Chem Soc, 2020, 142, 20744

[27] Wool R P. Self-healing materials: A review. Soft Matter, 2008, 4, 400

[28] Na S R, Kim Y, Lee C G, et al. Adhesion and self-healing between monolayer molybdenum disulfide and silicon oxide. Sci Rep, 2017, 7, 14740

[29] Zhang X K, Liao Q L, Kang Z, et al. Self-healing originated van der Waals homojunctions with strong interlayer coupling for high-performance photodiodes. ACS Nano, 2019, 13, 3280

[30] Ma Z, Huang P, Li J, et al. Multiferroicity and giant in-plane negative Poisson's ratio in wurtzite monolayers. Npj Comput Mater, 2022, 8, 1

[31] Kenji Y, Wang X R, Kenji W, et al. Stacking-engineered ferroelectricity in bilayer boron nitride. Science, 2021, 372(6549), 1458

[32] Vizner Stern M, Waschitz Y, Cao W, et al. Interfacial ferroelectricity by van der Waals sliding. Science, 2021, 372(6549), 1462

[33] Lee C G, Wei X D, Kysar J W, et al. Measurement of the elastic properties and intrinsic strength of monolayer graphene. Science, 2008, 321, 385

[34] Wu M H, Li J. Sliding ferroelectricity in 2D van der Waals materials: Related physics and future opportunities. Proc Natl Acad Sci U S A, 2021, 118, e2115703118

[35] Wu M H. Two-dimensional van der Waals ferroelectrics: Scientific and technological opportunities. ACS Nano, 2021, 15, 9229

[36] Li L, Wu M H. Binary compound bilayer and multilayer with vertical polarizations: Two-dimensional ferroelectrics, multiferroics, and nanogenerators. ACS Nano, 2017, 11, 6382

[37] Calderon S V, Hayden J, Baksa S M, et al. Atomic-scale polarization switching in wurtzite ferroelectrics. Science, 2023, 380, 1034

[38] Dronskowski R, Bloechl P E. Crystal orbital Hamilton populations (COHP): Energy-resolved visualization of chemical bonding in solids based on density-functional calculations. J Phys Chem, 1993, 97, 8617

[39] Xu C, Mao J F, Guo X Y, et al. Two-dimensional ferroelasticity in van der Waals β'-In$_2$Se$_3$. Nat Commun, 2021, 12, 3665

[40] Zhou J, Xu H W, Li Y F, et al. Opto-mechanics driven fast martensitic transition in two-dimensional materials. Nano Lett, 2018, 18, 7794

[41] Pan Y M, Zhou J. Toggling valley-spin locking and nonlinear optical properties of single-element multiferroic monolayers via light. Phys Rev Applied, 2020, 14, 014024

[42] Xu B, Li S C, Jiang K, et al. Switching of the magnetic anisotropy via strain in two dimensional multiferroic materials: CrSX (X = Cl, Br, I). Appl Phys Lett, 2020, 116, 052403

[43] Ma Y D, Kou L Z, Huang B B, et al. Two-dimensional ferroelastic topological insulators in single-layer Janus transition metal dichalcogenides MSSe (M = Mo, W). Phys Rev B, 2018, 98, 085420

[44] Zhang T, Liang Y, Xu X L, et al. Ferroelastic-ferroelectric multiferroics in a bilayer lattice. Phys Rev B, 2021, 103, 165420

[45] Li W B, Li J. Ferroelasticity and domain physics in two-dimensional transition metal dichalcogenide monolayers. Nat Commun, 2016, 7, 10843

[46] Kim K S, Zhao Y, Jang H, et al. Large-scale pattern growth of graphene films for stretchable transparent electrodes. Nature, 2009, 457, 706

[47] Bertolazzi S, Brivio J, Kis A. Stretching and breaking of ultrathin MoS$_2$. ACS Nano, 2011, 5, 9703

[48] Tao J, Shen W F, Wu S, et al. Mechanical and electrical anisotropy of few-layer black phosphorus. ACS Nano, 2015, 9, 11362

[49] Zhang X W, Liu Q H, Luo J W, et al. Hidden spin polarization in inversion-symmetric bulk crystals. Nat Phys, 2014, 10, 387

[50] Beaulieu S, Schusser J, Dong S, et al. Revealing hidden orbital pseudospin texture with time-reversal dichroism in photoelectron angular distributions. Phys Rev Lett, 2020, 125, 216404

[51] Tu J, Chen X B, Ruan X Z, et al. Direct observation of hidden spin

polarization in 2H–MoTe$_2$. Phys Rev B, 2020, 101, 035102

[52] Zhang K, Zhao S X, Hao Z Y, et al. Observation of spin-momentum-layer locking in a centrosymmetric crystal. Phys Rev Lett, 2021, 127, 126402

[53] Yao W, Wang E Y, Huang H Q, et al. Direct observation of spin-layer locking by local Rashba effect in monolayer semiconducting PtSe$_2$ film. Nat Commun, 2017, 8, 14216

[54] Cheng C, Sun J T, Chen X R, et al. Hidden spin polarization in the 1T-phase layered transition-metal dichalcogenides MX_2 (M = Zr, Hf; X = S, Se, Te). Sci Bull, 2018, 63, 85

[55] Yuan L D, Liu Q H, Zhang X W, et al. Uncovering and tailoring hidden Rashba spin–orbit splitting in centrosymmetric crystals. Nat Commun, 2019, 10, 1

[56] Liu Q H, Zhang X W, Jin H, et al. Search and design of nonmagnetic centrosymmetric layered crystals with large local spin polarization. Phys Rev B, 2015, 91, 235204

[57] Liu Q H, Guo Y Z, Freeman A J. Tunable rashba effect in two-dimensional LaOBiS$_2$ films: Ultrathin candidates for spin field effect transistors. Nano Lett, 2013, 13, 5264

[58] Zhang X T, Zhang F, Wang Y X, et al. Defect-controlled nucleation and orientation of WSe$_2$ on hBN: A route to single-crystal epitaxial monolayers. ACS Nano, 2019, 13, 3341

[59] Brown P D, Russell G J, Woods J. Anisotropic defect distribution in ZnSe/ZnS epitaxial layers grown by metalorganic vapor-phase epitaxy on (001)-oriented GaAs. J Appl Phys, 1989, 66, 129

[60] Han Y M, Li M Y, Jung G S, et al. Sub-nanometre channels embedded in two-dimensional materials. Nat Mater, 2018, 17, 129

[61] Jain S C, Willander M, Narayan J, et al. III–nitrides: Growth, characterization, and properties. J Appl Phys, 2000, 87, 965

[62] Xiao C C, Wang F, Yang S A, et al. Elemental ferroelectricity and antiferroelectricity in group-V monolayer. Adv Funct Mater, 2018, 28, 1707383

[63] Liu C, Gao R L, Cheng X L, et al. First-principles study of ferroelectricity, antiferroelectricity, and ferroelasticity in two-dimensional γ-AlOOH. Phys Rev B, 2023, 107, L121402

[64] Jiang K, Ji J P, Gong W B, et al. Mechanical cleavage of non-van der Waals structures towards two-dimensional crystals. Nat Synth, 2023, 2, 58

[65] Puthirath Balan A, Radhakrishnan S, Woellner C F, et al. Exfoliation of a non-van der Waals material from iron ore hematite. Nat Nanotechnol, 2018, 13, 602

[66] Wu H, Zhang W F, Yang L, et al. Strong intrinsic room-temperature ferromagnetism in freestanding non-van der Waals ultrathin 2D crystals. Nat Commun, 2021, 12, 5688

[67] Staudinger P, Moselund K E, Schmid H. Exploring the size limitations of wurtzite III–V film growth. Nano Lett, 2020, 20, 686

[68] Yue G H, Yan P X, Yan D, et al. Synthesis of two-dimensional micron-sized single-crystalline ZnS thin nanosheets and their photoluminescence properties. J Cryst Growth, 2006, 293, 428

[69] Wang L, Xiong K L, He Y K, et al. Epitaxial growth of wafer-scale two-dimensional polytypic ZnS thin films on ZnO substrates. Cryst Eng Comm, 2017, 19, 2294

[70] Wang Z W, Wen X D, Hoffmann R, et al. Reconstructing a solid-solid phase transformation pathway in CdSe nanosheets with associated soft ligands. Proc Natl Acad Sci USA, 2010, 107, 17119

[71] Wang C S, Ke X X, Wang J J, et al. Ferroelastic switching in a layered-perovskite thin film. Nat Commun, 2016, 7, 1

[72] Park M H, Kim H J, Kim Y J, et al. Toward a multifunctional monolithic device based on pyroelectricity and the electrocaloric effect of thin antiferroelectric Hf$_x$Zr$_{1-x}$O$_2$ films. Nano Energy, 2015, 12, 131

[73] Mischenko A S, Zhang Q, Scott J F, et al. Giant electrocaloric effect in thin-film PbZr$_{0.95}$Ti$_{0.05}$O$_3$. Science, 2006, 311, 1270

[74] Geng W P, Liu Y, Meng X J, et al. Giant negative electrocaloric effect in antiferroelectric La-doped Pb(ZrTi)O$_3$ thin films near room temperature. Adv Mater, 2015, 27, 3165

[75] Hao X H, Zhai J W, Kong L B, et al. A comprehensive review on the progress of lead zirconate-based antiferroelectric materials. Prog Mater Sci, 2014, 63, 1

[76] Bharadwaja S S N, Krupanidhi S B. Antiferroelectric thin films for MEMs applications. Ferroelectrics, 2001, 263, 39

[77] Xu B M, Cross L E, Bernstein J J. Ferroelectric and antiferroelectric films for microelectromechanical systems applications. Thin Solid Films, 2000, 377/378, 712

[78] Guo M Y, Wu M, Gao W W, et al. Giant negative electrocaloric effect in antiferroelectric PbZrO$_3$ thin films in an ultra-low temperature range. J Mater Chem C, 2019, 7, 617

Zhuang Ma got his bachelor's degree in 2017 from Zhoukou Normal University and his master's degree in 2020 from Zhengzhou University. Then, he got his PhD from Shenzhen University in 2023. Currently, he is a lecturer at Zhoukou Normal University. His research focuses on spintronics, ferroelectrics and optoelectronic materials.
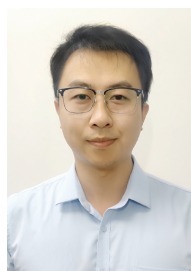
Pu Huang received his doctoral degree from Peking University, Beijing, China, in 2017. He is currently an Associate Professor at the College of Physics and Optoelectronic Engineering, Shenzhen University. His current research interests include high-throughput computing, design of phase change semiconductor, and development of DFT-based methodologies.